Coupling Analysis and Decoupling Design of Power and Voltage Loops for Single-Phase Grid-Forming Converters

Zicheng Zhang, *Student Member, IEEE*, Chenghui Zhang, *Fellow, IEEE*, Cheng Fu, and Jingyang Fang, *Senior Member, IEEE*

***Abstract*—In modern power systems, grid-forming converters (GFMCs) are recognized as a key enabling technology due to superior grid formation and supporting capabilities. Generally, the outerpower and innervoltage loops of GFMCs are designed independently for simplicity. However, the coupling between these two loops can cause severe performance degradation or even system instability. To address this problem, we propose a robust singular perturbation method for single-phase GFMCs (SPGFMCs), enabling quantitative coupling analysis and decoupling design of power and voltage loops. Specifically, the small-signal model of the SPGFMC is partitioned into slow and fast subsystems, with their dynamics corresponding to power and voltage loops, respectively. On this basis, two decoupling criteria are established to ensure system stability and performance. The criteria can also quantify the pointwise coupling between the two loops at each frequency. To facilitate decoupling, we further develop a design procedure using the criteria. The proposed criteria reveal that the power and voltage control loops can achieve stability-based and performance-based decoupling with comparable and threefold bandwidths, respectively, which is less conservative than the conventional tenfold bandwidth separation. Simulation and experimental results validate the effectiveness of theoretical analyses and decoupling control design.**

***Index Terms*—Decoupling design, power and voltage control, robust singular perturbation method, single-phase grid-forming converters (SPGFMCs).**

Received 22 July 2025; revised 8 October 2025; accepted 16 November 2025. Date of publication 25 November 2025; date of current version 25 February 2026. This work was supported in part by the National Natural Science Foundation of China under Grant 2022YFF0712700, Grant 62503261, Grant 20221017-9, Grant 62333013, Grant 52377192, and Grant 61821004, in part by the Shandong Provincial Natural Science Foundation under Grant ZR2025QC1565, in part by the National Natural Science Foundation of China under Grant Excellent Young Scientists Funding Program (Overseas), in part by the Research on the Evaluation of Grid-Integration Performance and Oscillation Risk Assessment Technology for Grid-Following/-Forming Renewable Energy Plants in Electric Power Research Institute 2025 Projects under Grant B311DS25Z007, and in part by the Qingdao Postdoctoral Program under Grant QDBSH20250101006. Recommended for publication by Associate Editor C.K. Tse. *(Corresponding authors: Chenghui Zhang; Jingyang Fang.)*

Zicheng Zhang, Chenghui Zhang, and Jingyang Fang are with the School of Control Science and Engineering, Shandong University, Jinan 250100, China (e-mail: zhangzicheng1991@mail.sdu.edu.cn; zchui@sdu.edu.cn; jingyangfang@sdu.edu.cn).

Cheng Fu is with the School of Automation, Qingdao University, Qingdao 266071, China (e-mail: cfu@mail.sdu.edu.cn).

Color versions of one or more figures in this article are available at https://doi.org/10.1109/TPEL.2025.3636900.

Digital Object Identifier 10.1109/TPEL.2025.3636900

NOMENCLATURE

Abbreviations

GFMC	Grid-forming converter.
SPGFMC	Single-phase GFMC.
TPGFMC	Three-phase GFMC.
SPT	Singular perturbation theory.
LPF	Low-pass filter.
PI	Proportional-integral.
PR	Proportional resonant.

Parameters and Variables

$V_{\mathrm{s}}, \theta_{\mathrm{s}}$	Grid voltage amplitude and phase angle.
θ_{g}	Converter phase angle.
δ_{p}	Power angle.
ω_0	Fundamental angular frequency.
T_0	Fundamental period.
V_{ref}	Reference voltage amplitude.
$\mathbf{x}_{\mathrm{pdq}}$	$[i_{\mathrm{gid}}, i_{\mathrm{giq}}, v_{\mathrm{gfd}}, v_{\mathrm{gfq}}, i_{\mathrm{ggd}}, i_{\mathrm{ggq}}]^{\mathrm{T}}$, converter plant states.
ω_{clp}	Cut-off frequency of the first-order LPF.
k_{ppg}	Droop coefficient of the active power controller.
$k_{\mathrm{pqg}}, k_{\mathrm{iqg}}$	Proportional and integral coefficients of the reactive power controller.
$k_{\mathrm{pvc}}, k_{\mathrm{rvc}}$	Proportional and resonant coefficients of the voltage PR controller.
k_{iff}	Grid-side current feedforward coefficient of the voltage controller.
$k_{\mathrm{pic}}, k_{\mathrm{vff}}$	Proportional and capacitor voltage feedforward coefficients of the current controller.
$\mathbf{G}_{\mathrm{p}}(s)$	Converter plant Laplacian matrix.
$G_{\mathrm{d}}(s)$	Time delay transfer function.
$\mathbf{K}_{\mathrm{vpr}}(s)$	Laplacian matrix of the voltage PR regulator.
$\mathbf{C}_{\mathrm{pcal}}$	Power calculation matrix.
$F_{\mathrm{lp}}(s)$	Low-pass filter transfer function.
$F_{\mathrm{d}}(s)$	Transfer function of $[1 + \eta(\cdot)]/2$.
$\mathbf{y}_{\mathrm{ipqg}}$	Defined as $\mathbf{C}_{\mathrm{pcal}}\mathbf{x}_{\mathrm{pdq}}$.
$\mathbf{y}_{\mathrm{pqg}}$	$[p_{\mathrm{g}}, q_{\mathrm{g}}]^{\mathrm{T}}$, active and reactive power.
$\mathbf{y}_{\mathrm{pqgf}}$	$[p_{\mathrm{gf}}, q_{\mathrm{gf}}]^{\mathrm{T}}$, active and reactive power after LPFs.
$\mathbf{K}_{\mathrm{pow}}(s)$	Power controller Laplacian matrix.
$\mathbf{C}_{\mathrm{vref}}$	Voltage reference calculation matrix.
$\mathbf{G}_{\mathrm{ic}}(s)$	Current control loop Laplacian matrix.

$\mathbf{G}_{\mathrm{vc}}(s)$	Voltage control loop Laplacian matrix.
$\mathbf{G}_{\mathrm{pc}}(s)$	Power control loop Laplacian matrix.
$\mathbf{G}_{\mathrm{vc0}}$	Steady-state gain matrix of $\mathbf{G}_{\mathrm{vc}}(s)$.
$\Delta\mathbf{G}_{\mathrm{vc}}(s)$	$\mathbf{G}_{\mathrm{vc}}(s)-\mathbf{G}_{\mathrm{vc0}}$, dynamic components of $\mathbf{G}_{\mathrm{vc}}(s)$.
$\mathbf{G}_{\mathrm{slow}}(s)$	Slow subsystem, the reduced-order approximation of $\mathbf{G}_{\mathrm{pc}}(s)$.
$\mathbf{G}_{\mathrm{fast}}(s)$	Fast subsystem.
$\mathbf{G}_{\mathrm{loop}}(s)$	$\mathbf{G}_{\mathrm{fast}}(s)\mathbf{G}_{\mathrm{slow}}(s)$, loop Laplacian matrix.
$\mathbf{I}_{\mathrm{n}}$	Identity matrix of dimension n.
$\mathbf{0}_{\mathrm{m\times n}}$	Zero matrix of dimension $m\times n$.

Prefix

Δ	Small-signal perturbation.

Superscripts

-1, T	Inverse and transposition of a matrix.

Subscripts

α, β	Variables in α-axis and β-axis.
d, q	Variables in d-axis and q-axis.
0	Values in steady-state condition.
ref	Reference values.

Matrix index

(m, n)	Row and column indices of a matrix.

Operators

$\eta(\cdot)$	$T_0/4$ delay operator.
$\|\cdot\|_\infty$	H_∞ norm of a Laplacian matrix.
$\sigma_{\max}(\cdot)$	Maximum singular value of a matrix.

I. Introduction

DRIVEN by the increasing global energy demand, the installed capacity of renewable energy worldwide has continued to grow steadily. In the fields of photovoltaics, wind power, and battery energy storage, power converters serve as indispensable components to secure grid connections [1]. Generally, power converters are controlled as either ac current or ac voltage sources, which are recognized as grid-following converters (GFLCs) or GFMCs, respectively [2]. Compared to GFLCs, GFMCs possess inherent grid-formulation capabilities. Moreover, they eliminate the need for phase-locked loops and allow both islanded and grid-tied operations [3]. Besides, GFMCs exhibit superior stability to GFLCs in a weak grid with a low short-circuit ratio [4], [5]. With these advantages, GFMCs are regarded as a key technology in modern power systems [6].

In engineering, TPGFMCs and SPGFMCs can be employed. TPGFMCs offer higher output power, whereas SPGFMCs benefit from small size and easy maintenance, making them suitable for residential scenarios. For both GFMCs, the basic control objective lies in power and voltage regulation, which are realized by the power and voltage controllers, respectively [7]. The power controller provides voltage amplitude and phase-angle references for the voltage controller, thereby forming a cascaded control structure [8]. For active power control, the droop control strategy enables desired power sharing between converter units without communication [9]. The virtual synchronous machine control approach provides inertia and damping as synchronous generators to support power grids [10]. Virtual oscillator control replicates the behavior of a nonlinear oscillator to achieve self-synchronization [11]. As for reactive power control, the droop method and the PI regulator are commonly used [12]. The former allows autonomous reactive power sharing, while the latter achieves zero steady-state error tracking. In addition, constant voltage control, which directly regulates the ac voltage amplitude and removes the reactive power controller, is also expected in GFMCs according to IEEE Std. 2800−2022 [13].

The innerloop voltage controller aims to track the reference amplitude and phase angle of ac capacitor voltages. Existing voltage control frameworks typically comprise dual-loop and single-loop structures [14]. The dual-loop voltage control, which includes an ac voltage controller and an ac current controller, is a common structure [15]. In this case, the ac voltage controller yields the ac current reference, which is subsequently regulated by the current controller. Additionally, the capacitor voltage and grid current feedforward can, respectively, be employed in the voltage and current controllers to improve the performance of GFMCs [16]. The dual-loop control provides superior current regulation at the cost of increased complexity. In comparison, the single-loop voltage control features a simpler structure and benefits from improved control dynamics [17]. However, the current regulation is excluded from this control structure.

As discussed previously, the control of GFMCs involves a power loop and an ac voltage (or voltage-current) loop, leading to increased complexity in system analysis and controller design. For simplicity, the outerloop power and innerloop voltage controllers are often designed independently [18]. For power controller design, the voltage loop dynamics are neglected, assuming they are much faster than those of the power loop. In other words, the power controller is designed using a reduced-order model [19]. In parallel, for voltage controller design, the power controller is ignored, and the voltage reference is fixed. However, the two control loops are essentially coupled. As reported in [19], dual-loop voltage control can easily cause undesirable power oscillations in the grid-tied mode, thus indicating considerable couplings between power and voltage loops. In [20], it is validated that the improper design of control parameters results in inaccurate reduced-order models. Later, we theoretically reveal that GFMCs can be unstable even if the power and voltage loops are individually stable.

One famous tool for analyzing the coupling problem is the SPT [21]. Using this theory, the states of a full-order system are separated into slow and fast states according to their time scales. Accordingly, the system is transformed into reduced-order slow and fast subsystems, thereby simplifying the analysis. In the early stage, the SPT mainly applies to bulky power systems [22]. Currently, it has been extended to power converters and microgrids [23], [24], [25], [26], [27], [28], [29].

In [23], the SPT is employed in transient stability analysis of power converters under weak grid conditions. However, the

coupling between slow and fast subsystems is neglected. In [24], a two-time-scale voltage controller design method for GFMCs is presented, while the power controller is not considered. Cai et al. [25] proposed a singular-perturbation-based design method for SPGFMCs. Although it brings simplicity, it relies on qualitative bandwidth separation and lacks a quantitative criterion to ensure stability. In [26], the SPT is employed for the controller design of series-connected PV-powered GFMCs. However, the decoupling of power and voltage loops has not been addressed. Except for controller design, Rasheduzzaman et al. [27] and Mariani et al. [28] focused on deriving reduced-order models for microgrids using SPT to improve computation efficiency. Nayak et al. [29] further analyzed the convergence behavior of the inverter-based microgrid based on the SPT. However, these references mainly focus on system simplification and lack coupling analysis and decoupling design methodology between the power and voltage loops.

Typically, conventional SPT requires identifying a sufficiently small perturbation parameter [23], [25]. To ensure the stability of a full-order system, the upper bound of the perturbation parameter should be computed [30]. However, these metrics cannot quantify the coupling effect between power and voltage loops, and it is also challenging to derive a relevant decoupling criterion using the perturbation parameter. Moreover, the computation of this upper bound primarily aims to guarantee the stability of the full-order system, while the performance of converters is usually overlooked [30]. This article shows that decoupling based solely on stability considerations may cause remarkable performance degradation and yield inaccurate reduced-order models.

In addition to SPT, other coupling analysis methodologies have also been reported in [31], [32], [33], [34], [35], [36], and [37]. In [31], the participation factor analysis method is adopted to evaluate the impact of inner control loops. In [32], the coupling between outer and inner control loops is investigated using the eigenvalue analysis approach. However, in both methods, the coupling effect between the outer and inner control loops is assessed primarily through the similarity of eigenvalues or time-domain response curves. No explicit mathematical criteria are provided to serve as quantitative metrics for decoupling design. Kabalan et al. [33] presented a Lyapunov-based method for stability analysis and attraction domain estimation of GFMCs when neglecting fast dynamics. However, the construction of Lyapunov functions is difficult for high-order systems. D'Arco et al. [34], [35] provided the parametric sensitivity analysis method and a corresponding automatic tuning method of cascaded controllers for multiloop GFMCs, driving all poles to stability. Although effective, they fail to achieve decoupling between control loops and cannot yield accurate reduced-order models. In [36], the coupling between outer and inner loops is mitigated using bandwidth separation. Typically, a tenfold bandwidth difference is required, which may cause conservatism [35]. Liu et al. [37] offered a direct decoupling control method, removing the ac voltage controller. However, this method fails to address the resonant problem of *LCL* filters and does not apply to unbalanced grid conditions due to the absence of closed-loop controllers.

According to the literature review, there are research gaps on coupling analysis and decoupling design between power and voltage control loops, and more effective tools are expected. In this article, we propose a robust singular perturbation method and apply it to SPGFMCs for validation. First, the full-order small-signal models of SPGFMCs are derived and formulated as interconnected slow and fast systems. Then, two quantitative decoupling criteria, which comprise a marriage of the SPT and robust control theory, are proposed. The main contributions of this article are outlined as follows.

1) We propose a robust singular perturbation method for SPGFMCs, enabling effective decoupling between power and voltage control loops.
2) We establish the stability-based and performance-based criteria for decoupling, which allow the evaluation of the pointwise coupling at each frequency.
3) We theoretically reveal that the power and voltage control loops can achieve stability-based and performance-based decoupling with comparable and threefold bandwidths, respectively.
4) We develop a decoupling procedure using the criteria, enabling independent design of the two control loops and achieving satisfactory control performance.

The rest of this article is organized as follows. Section II introduces the small-signal models of SPGFMCs in the virtual $dq0$ frame. Section III performs a time-scale analysis of the SPGFMC model using the SPT and proposes the robust singular perturbation method. Section IV further presents a systematic analysis of the coupling between power and voltage loops and provides the procedure for decoupled controller design. Section V performs simulation and experimental validations for the proposed method. Finally, Section VI concludes this article.

II. System Description and Small-Signal Modeling of SPGFMCs

This section first introduces the schematics and control structure of SPGFMCs. Then, the small-signal models of SPGFMCs are established in the virtual $dq0$ frame.

A. Schematics and Control Structure

Fig. 1 shows the schematics of an SPGFMC. An *LCL* filter formed by L_{gi}, C_{gf}, and L_{gg} is employed to attenuate voltage and current harmonics. The power grid is modeled by a voltage source v_{s}, an inductor L_{s}, and a resistor R_{s}, where V_{s} and θ_{s} denote the grid voltage amplitude and phase angle, respectively. v_{g} is the voltage at the point of common coupling. i_{gi} and i_{gg} are the converter and grid currents, respectively. v_{gdc}, v_{gi}, and v_{gf} denote the dc-link, converter, and ac capacitor voltages. In Fig. 1, the subscript ref indicates reference variables.

Fig. 1 also describes a commonly used control diagram of SPGFMCs. The active and reactive power, denoted by p_{g} and q_{g}, are controlled using a droop controller and a PI regulator, respectively. The LPFs attenuate harmonics in p_{g} and q_{g}, yielding the filtered signals p_{gf} and q_{gf}. V_{ref0} and V_{ref} are the nominal and reference voltage amplitudes, respectively. ω_0

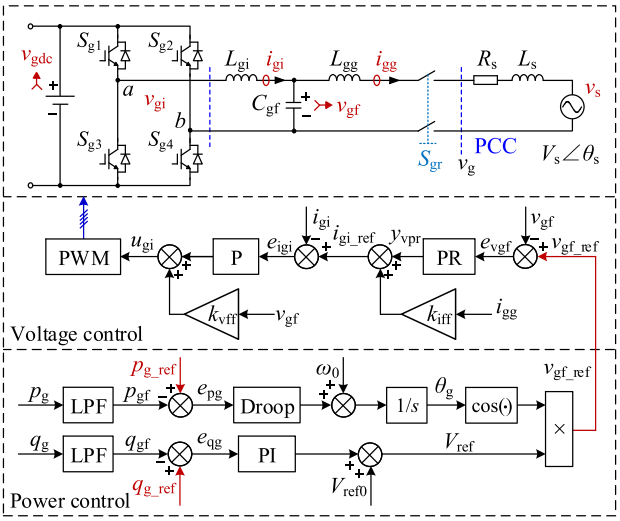

Fig. 1. Schematics and control diagram of SPGFMCs.

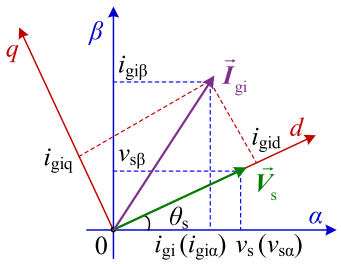

Fig. 2. Illustration of virtual $\alpha\beta0$ and $dq0$ frames.

denotes the line angular frequency. For ac voltage and current control, PR and proportional (P) regulators are adopted, respectively. Besides, an ac capacitor voltage feedforward term and a grid current feedforward term are also included to enhance the control performance. k_{vff} and k_{iff} denote the voltage and current feedforward coefficients. u_{gi} represents the current controller output.

B. Small-Signal Modeling of the Voltage Loop

For SPGFMCs, the output voltage and current are sinusoidal, making it inconvenient to derive the linearized small-signal model. Alternatively, the virtual $\alpha\beta0$ and $dq0$ frames can be introduced, as depicted in Fig. 2 [38]. In the virtual $dq0$ frame, the steady-state voltage and current appear as dc quantities, facilitating small-signal modeling. In Fig. 2, the subscripts α, β, d, and q represent variables in respective axes. $\vec{V}_s$ and $\vec{I}_{gi}$ are the virtual space vectors of v_s and i_{gi}, respectively. The α-axis coordinates correspond to real ac voltages and currents, while the virtual β-axis coordinates lag the respective α-axis coordinates by $\pi/2$. Then, the virtual dq-axis coordinates are further derived by applying the $\alpha\beta0$/$dq0$ transformation with a rotating angle θ_s [39].

1) System Plant Modeling: According to [38] and [39], the small-signal model of the system plant in the virtual $dq0$ frame can be derived as

$$\begin{aligned}
&L_{gi}\frac{d}{dt}\begin{bmatrix}\Delta i_{gid}\Delta i_{giq}\end{bmatrix}\\
&=\begin{bmatrix}0 & \omega_0 L_{gi}\\ -\omega_0 L_{gi} & 0\end{bmatrix}\begin{bmatrix}\Delta i_{gid}\\ \Delta i_{giq}\end{bmatrix}-\begin{bmatrix}\Delta v_{gfd}\\ \Delta v_{gfq}\end{bmatrix}+\begin{bmatrix}\Delta v_{gid}\\ \Delta v_{giq}\end{bmatrix}\\
&L_{gs}\frac{d}{dt}\begin{bmatrix}\Delta i_{ggd}\\ \Delta i_{ggq}\end{bmatrix}\\
&=\begin{bmatrix}-R_s & \omega_0 L_{gs}\\ -\omega_0 L_{gs} & -R_s\end{bmatrix}\begin{bmatrix}\Delta i_{ggd}\\ \Delta i_{ggq}\end{bmatrix}+\begin{bmatrix}\Delta v_{gfd}\\ \Delta v_{gfq}\end{bmatrix}-\begin{bmatrix}\Delta V_s\\ 0\end{bmatrix}\\
&C_{gf}\frac{d}{dt}\begin{bmatrix}\Delta v_{gfd}\\ \Delta v_{gfq}\end{bmatrix}\\
&=\begin{bmatrix}0 & \omega_0 C_{gf}\\ -\omega_0 C_{gf} & 0\end{bmatrix}\begin{bmatrix}\Delta v_{gfd}\\ \Delta v_{gfq}\end{bmatrix}+\begin{bmatrix}\Delta i_{gid}\\ \Delta i_{giq}\end{bmatrix}-\begin{bmatrix}\Delta i_{ggd}\\ \Delta i_{ggq}\end{bmatrix}
\end{aligned}\tag{1}$$

where the prefix Δ represents the small-signal perturbations, in this article, $L_{gs} = L_{gg}+L_s$. For simplicity, we define $\mathbf{v}_{gidq} = [v_{gid}, v_{giq}]^T$, $\mathbf{i}_{gidq} = [i_{gid}, i_{giq}]^T$, $\mathbf{v}_{gfdq} = [v_{gfd}, v_{gfq}]^T$, $\mathbf{i}_{ggdq} = [i_{ggd}, i_{ggq}]^T$, and $\mathbf{x}_{pdq} = [\mathbf{i}_{gidq}{}^T, \mathbf{v}_{gfdq}{}^T, \mathbf{i}_{ggdq}{}^T]^T$. The Laplacian (transfer function) matrix from $\Delta\mathbf{v}_{gidq}$ to $\Delta\mathbf{x}_{pdq}$ is denoted as $\mathbf{G}_p(s)$.

2) Current Controller Modeling: In the virtual $dq0$ frame, the small-signal model of the current controller is expressed as

$$\Delta\mathbf{u}_{gidq} = k_{pic}\left(\Delta\mathbf{i}_{gidq\_ref} - \Delta\mathbf{i}_{gidq}\right) + k_{vff}\Delta\mathbf{v}_{gfdq} \tag{2}$$

where $\mathbf{u}_{gidq} = [u_{gid}, u_{giq}]^T$ denote the current controller outputs in the virtual $dq0$ frame and k_{pic} is the proportional gain.

3) Time-Delay Modeling: In SPGFMCs, time delays are introduced by the duty ratio computation and pulsewidth modulation update. For a switching period of T_s, the equivalent time delay equals $1.5T_s$. The relationship between $\mathbf{v}_{gidq}$ and $\mathbf{u}_{gidq}$ is expressed as [40]

$$\mathbf{v}_{gidq} = G_d(s)\mathbf{u}_{gidq} = e^{-s1.5T_s}\mathbf{u}_{gidq} \approx \frac{1-0.75T_s s}{1+0.75T_s s}\mathbf{u}_{gidq}. \tag{3}$$

4) Voltage Controller Modeling: By applying the $\alpha\beta0$/$dq0$ transformation shown in [39], the state-space representation of the voltage PR regulator in the virtual $dq0$ frame is derived as

$$\begin{aligned}
\frac{d}{dt}\mathbf{x}_{vprdq} &= \begin{bmatrix}0 & \omega_0 & 1 & 0\\ -\omega_0 & 0 & 0 & 1\\ -\omega_0^2 & 0 & -2\omega_{cr} & \omega_0\\ 0 & -\omega_0^2 & -\omega_0 & -2\omega_{cr}\end{bmatrix}\mathbf{x}_{vprdq}+\begin{bmatrix}0 & 0\\ 0 & 0\\ 1 & 0\\ 0 & 1\end{bmatrix}\mathbf{e}_{vgfdq}\\
\mathbf{y}_{vprdq} &= 2k_{rvc}\omega_{cr}\begin{bmatrix}0 & 0 & 1 & 0\\ 0 & 0 & 0 & 1\end{bmatrix}\mathbf{x}_{vprdq}+k_{pvc}\mathbf{e}_{vgfdq}
\end{aligned}\tag{4}$$

where $\mathbf{x}_{vprdq}$ and $\mathbf{y}_{vprdq}$ denote the state and output vectors of the PR regulator, k_{pvc} and k_{rvc} are the proportional and resonant coefficients, respectively, and ω_{cr} denotes the damping factor.

Denoting $\mathbf{K}_{vpr}(s)$ as the small-signal Laplacian (transfer function) matrix of the voltage PR regulator, the ac voltage controller in the virtual $dq0$ frame is expressed as

$$\Delta\mathbf{i}_{gidq\_ref} = \mathbf{K}_{vpr}(s)\left(\Delta\mathbf{v}_{gfdq\_ref} - \Delta\mathbf{v}_{gfdq}\right) + k_{iff}\Delta\mathbf{i}_{ggdq}. \tag{5}$$

C. Small-Signal Modeling of the Power Loop

1) Power Controller Modeling: According to [40], the small-signal model of the power controllers is expressed as

$$\begin{cases} \Delta\delta_{\mathrm{p}} = k_{\mathrm{ppg}}\left(\Delta p_{\mathrm{g\_ref}} - \Delta p_{\mathrm{g}}\right)/s \\ \Delta V_{\mathrm{ref}} = \left(k_{\mathrm{pqg}} + k_{\mathrm{iqg}}/s\right)\left(\Delta q_{\mathrm{g\_ref}} - \Delta q_{\mathrm{g}}\right) \end{cases} \tag{6}$$

where $\delta_{\mathrm{p}} = \theta_{\mathrm{g}} - \theta_{\mathrm{s}}$ represents the power angle, k_{ppg} is the droop coefficient of the active power controller, and k_{pqg} and k_{iqg} are the proportional and integral coefficients of the reactive power controller, respectively.

In this article, the Laplacian matrix of the power controller is denoted as $\mathbf{K}_{\mathrm{pow}}(s)$.

2) Voltage Reference Modeling: According to [40], the *dq*-axis voltage references $v_{\mathrm{gfd^*ref}}$ and $v_{\mathrm{gfd^*ref}}$ are calculated in terms of V_{ref} and δ_{p} as

$$\begin{cases} v_{\mathrm{gfd\_ref}} = V_{\mathrm{ref}}\cos\delta_{\mathrm{p}} \\ v_{\mathrm{gfq\_ref}} = V_{\mathrm{ref}}\sin\delta_{\mathrm{p}} \end{cases}. \tag{7}$$

Subsequently, its small-signal model is derived as

$$\begin{bmatrix} \Delta v_{\mathrm{gfd\_ref}} \\ \Delta v_{\mathrm{gfq\_ref}} \end{bmatrix} = \begin{bmatrix} -V_{\mathrm{ref0}}\sin\delta_{\mathrm{p0}} & \cos\delta_{\mathrm{p0}} \\ V_{\mathrm{ref0}}\cos\delta_{\mathrm{p0}} & \sin\delta_{\mathrm{p0}} \end{bmatrix} \begin{bmatrix} \Delta\delta_{\mathrm{p}} \\ \Delta V_{\mathrm{ref}} \end{bmatrix} \tag{8}$$

where V_{ref0} and δ_{p0} are the steady-state values of V_{ref} and δ_{p}, respectively. For convenience, the coefficient matrix in (8) is denoted as $\mathbf{C}_{\mathrm{vref}}$.

3) Power Calculation Modeling: Based on [42], the active power and reactive power of SPGFMCs can be calculated as

$$\begin{cases} p_{\mathrm{g}} = \frac{1}{2}\left[v_{\mathrm{gf}} i_{\mathrm{gg}} + \eta(v_{\mathrm{gf}})\eta(i_{\mathrm{gg}})\right] \\ q_{\mathrm{g}} = \frac{1}{2}\left[\eta(v_{\mathrm{gf}}) i_{\mathrm{gg}} - v_{\mathrm{gf}}\eta(i_{\mathrm{gg}})\right] \end{cases} \tag{9}$$

where $\eta(\cdot)$ represents a $T_0/4$ delay operator, with $T_0 = 2\pi/\omega_0$ denoting the fundamental period.

By applying the $\alpha\beta0/dq0$ transformation on (9), p_{g} and q_{g} can be further expressed as

$$\begin{cases} p_{\mathrm{g}} = \frac{1}{4}\left[v_{\mathrm{gfd}} i_{\mathrm{ggd}} + v_{\mathrm{gfq}} i_{\mathrm{ggq}} + \eta(v_{\mathrm{gfd}})\eta(i_{\mathrm{ggd}}) + \eta(v_{\mathrm{gfq}})\eta(i_{\mathrm{ggq}})\right] + p_{\mathrm{g2}} \\ q_{\mathrm{g}} = \frac{1}{4}\left[\eta(v_{\mathrm{gfq}}) i_{\mathrm{ggd}} - \eta(v_{\mathrm{gfd}}) i_{\mathrm{ggq}} - v_{\mathrm{gfd}}\eta(i_{\mathrm{ggq}}) + v_{\mathrm{gfq}}\eta(i_{\mathrm{ggd}})\right] + q_{\mathrm{g2}} \end{cases} \tag{10}$$

where p_{g2} and q_{g2} represent the double-line-frequency power components introduced by the power calculation. Detailed derivations are given in the Appendix.

In SPGFMCs, p_{g2} and q_{g2} should be suppressed to avoid double-line-frequency power oscillations. In this article, it is accomplished using two LPFs, as shown in Fig. 1. Accordingly, p_{g2} and q_{g2} can be neglected in modeling, and the small-signal model of the power calculation is derived as

$$\Delta\mathbf{y}_{\mathrm{pqg}} = F_{\mathrm{d}}(s)\mathbf{C}_{\mathrm{pcal}}\Delta\mathbf{x}_{\mathrm{pdq}} \tag{11}$$

where $\mathbf{y}_{\mathrm{pqg}} = [p_{\mathrm{g}}, q_{\mathrm{g}}]^{\mathrm{T}}$. $F_{\mathrm{d}}(s)$ represents the transfer function of $[1 + \eta(\cdot)]/2$, and $\mathbf{C}_{\mathrm{pcal}}$ is expressed as

$$\mathbf{C}_{\mathrm{pcal}} = \frac{1}{2}\begin{bmatrix} 0 & 0 & I_{\mathrm{ggd0}} & I_{\mathrm{ggq0}} & V_{\mathrm{gfd0}} & V_{\mathrm{gfq0}} \\ 0 & 0 & -I_{\mathrm{ggq0}} & I_{\mathrm{ggd0}} & V_{\mathrm{gfq0}} & -V_{\mathrm{gfd0}} \end{bmatrix} \tag{12}$$

where V_{gfd0}, V_{gfq0}, I_{ggd0}, and I_{ggq0} denote the steady-state values of v_{gfd}, v_{gfq}, i_{ggd}, and i_{ggq}, respectively.

Additionally, the transfer function of LPFs takes the form of

$$F_{\mathrm{lp}}(s) = \left[\omega_{\mathrm{clp}}/\left(s + \omega_{\mathrm{clp}}\right)\right]^2 \tag{13}$$

where ω_{clp} is the cut-off frequency of a first-order LPF.

Fig. 3 shows the complete small-signal block diagram of the above models, where $\mathbf{y}_{\mathrm{ipqg}} = \mathbf{C}_{\mathrm{pcal}}\mathbf{x}_{\mathrm{pdq}}$ and $\mathbf{y}_{\mathrm{pqgf}} = [p_{\mathrm{gf}}, q_{\mathrm{gf}}]^{\mathrm{T}}$. The Laplacian matrices $\mathbf{G}_{\mathrm{ic}}(s)$, $\mathbf{G}_{\mathrm{vc}}(s)$, and $\mathbf{G}_{\mathrm{pc}}(s)$ denote the current, voltage, and power control loops, respectively. The detailed derivations of their expressions are elaborated in the Appendix.

Through manipulation, Fig. 3 is further simplified to Fig. 4. As shown, the analyses are performed within a multiple-input multiple-output framework, without neglecting any interchannel coupling. In this article, we use the notation (m, n) to represent the matrix element in the mth row and nth column. Consequently, $\mathbf{G}_{\mathrm{vc}}(s)(3, 1)$ and $\mathbf{G}_{\mathrm{vc}}(s)(4, 2)$ denote the d-axis and q-axis voltage transfer functions. $\mathbf{G}_{\mathrm{pc}}(s)(1, 1)$ and $\mathbf{G}_{\mathrm{pc}}(s)(2, 2)$ represent the active and reactive power transfer functions, respectively.

III. Robust Singular Perturbation Method for Decoupling of Power and Voltage Loops

In this section, we first perform a time-scale analysis of SPGFMCs, drawing on the idea of the conventional SPT. Then, we present the proposed robust singular perturbation method.

A. Conventional Singular Perturbation Theory

Consider a linear singularly perturbed system [21]

$$\frac{\mathrm{d}}{\mathrm{d}t}\mathbf{x}_{\mathrm{s}} = \mathbf{A}_{11}\mathbf{x}_{\mathrm{s}} + \mathbf{A}_{12}\mathbf{z}_{\mathrm{f}} + \mathbf{B}_1\mathbf{u}_{\mathrm{in}} \tag{14a}$$

$$\varepsilon\frac{\mathrm{d}}{\mathrm{d}t}\mathbf{z}_{\mathrm{f}} = \mathbf{A}_{21}\mathbf{x}_{\mathrm{s}} + \mathbf{A}_{22}\mathbf{z}_{\mathrm{f}} + \mathbf{B}_2\mathbf{u}_{\mathrm{in}} \tag{14b}$$

where ε denotes a small perturbation parameter, $\mathbf{x}_{\mathrm{s}}$ and $\mathbf{z}_{\mathrm{f}}$ are identified as the slow and fast states, $\mathbf{u}_{\mathrm{in}}$ are system inputs, and $\mathbf{A}_{11}$, $\mathbf{A}_{12}$, $\mathbf{A}_{21}$, $\mathbf{A}_{22}$, $\mathbf{B}_{11}$, and $\mathbf{B}_{12}$ are coefficient matrices.

Ignoring the dynamics of the fast states in (14b), we obtain the steady-state values of $\mathbf{z}_{\mathrm{f}}$ as $\mathbf{z}_{\mathrm{f0}} = -\mathbf{A}_{22}{}^{-1}\mathbf{A}_{21}\mathbf{x}_{\mathrm{s}} - \mathbf{A}_{22}{}^{-1}\mathbf{B}_2\mathbf{u}_{\mathrm{in}}$, with $\mathbf{A}_{22}$ being nonsingular. Then, $\mathbf{z}_{\mathrm{f}}$ are decomposed into

$$\mathbf{z}_{\mathrm{f}} = \mathbf{z}_{\mathrm{f0}} + \mathbf{z}_{\mathrm{f}\Delta} \tag{15}$$

where $\mathbf{z}_{\mathrm{f}\Delta}$ denote the dynamic components of $\mathbf{z}_{\mathrm{f}}$.

When ε is sufficiently small, $\mathbf{z}_{\mathrm{f}\Delta}$ can be omitted in (14a), and a slow reduced-order subsystem is derived as

$$\frac{\mathrm{d}}{\mathrm{d}t}\mathbf{x}_{\mathrm{s}} = \mathbf{A}_0\mathbf{x}_{\mathrm{s}} + \mathbf{B}_0\mathbf{u}_{\mathrm{in}} \tag{16}$$

where $\mathbf{A}_0 = \mathbf{A}_{11} - \mathbf{A}_{12}\mathbf{A}_{22}{}^{-1}\mathbf{A}_{21}$, $\mathbf{B}_0 = \mathbf{B}_1 - \mathbf{A}_{12}\mathbf{A}_{22}{}^{-1}\mathbf{B}_2$.

Substituting (15) into (14b), a fast subsystem is obtained as

$$\varepsilon\frac{\mathrm{d}}{\mathrm{d}t}\mathbf{z}_{\mathrm{f}\Delta} = \mathbf{A}_{22}\mathbf{z}_{\mathrm{f}\Delta} - \varepsilon\frac{\mathrm{d}}{\mathrm{d}t}\mathbf{z}_{\mathrm{f0}}. \tag{17}$$

For a sufficiently small ε, the term $\varepsilon\mathrm{d}\mathbf{z}_{\mathrm{f0}}/\mathrm{d}t$ can be neglected, and (17) is simplified as

$$\varepsilon\frac{\mathrm{d}}{\mathrm{d}t}\mathbf{z}_{\mathrm{f}\Delta} = \mathbf{A}_{22}\mathbf{z}_{\mathrm{f}\Delta}. \tag{18}$$

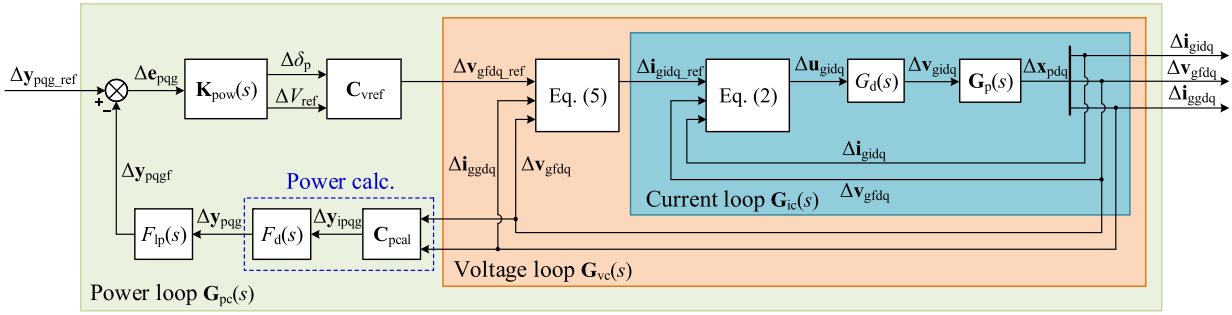

Fig. 3. Small-signal models of SPGFMCs.

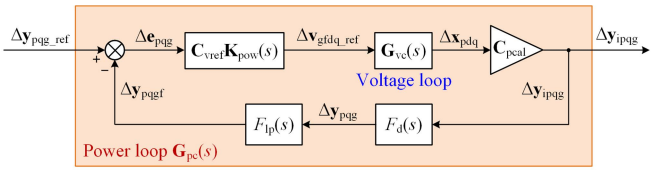

Fig. 4. Simplified block diagram of the small-signal models.

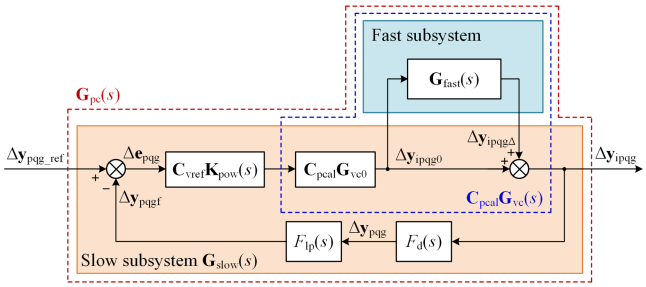

Fig. 5. Reformulation of the SPGFMC model using the SPT.

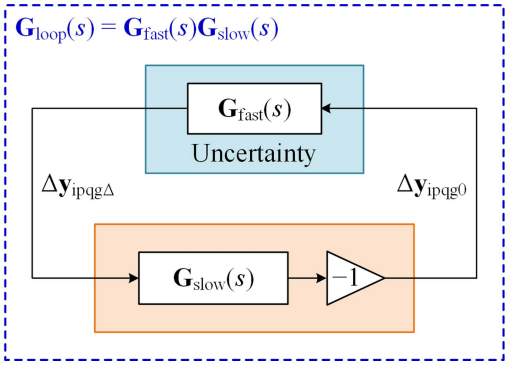

Fig. 6. Equivalent block diagram of SPGFMC when $\Delta\mathbf{y}_{pqgf\_ref}$ are zeros.

As observed, the full-order system shown in (14a) and (14b) is decomposed into two independent slow and fast subsystems, and its stability is guaranteed by individual stabilities of the two subsystems for a sufficiently small ε [21]. Therefore, the analysis of the full-order system can be simplified.

B. Time-Scale Analysis of SPGFMCs

Inspired by the idea of the SPT, we now aim to analyze the time-scale property of SPGFMCs to address the decoupling of the power and voltage loops. In general, the application of conventional SPT requires the parameter ε to be sufficiently small. As described in Section I, this leads to incompatibility with the decoupling analysis and design.

In contrast, we perform the time-scale analysis of SPGFMCs without the need to identify the parameter ε. Specifically, we treat the states of the innervoltage loop, i.e., the states of $\mathbf{G}_{vc}(s)$, as the fast states. The remaining states are recognized as the slow states. In the frequency domain, neglecting the dynamics of fast states is equivalent to retaining only the steady-state gain matrix of the voltage loop. Therefore, $\mathbf{G}_{vc}(s)$ is decomposed into

$$\mathbf{G}_{vc}(s) = \mathbf{G}_{vc0} + \Delta\mathbf{G}_{vc}(s) \tag{19}$$

where $\mathbf{G}_{vc0}$ denotes the steady-state gain matrix of $\mathbf{G}_{vc}(s)$, and $\Delta\mathbf{G}_{vc}(s)$ captures its dynamic components.

By applying (19) in Fig. 4, an equivalent representation can be obtained in Fig. 5, where the slow and fast subsystems are

TABLE I
PARAMETERS OF THE SYSTEM PLANT

Descriptions	SYMBOLS	Values
Dc-bus voltage	v_{gdc}	400 V
Grid voltage amplitude	V_s	155 V
Line angular frequency	ω_0	$2\pi\cdot50$ rad/s
Switching frequency	f_s	16 kHz
Filter inductances	L_{gi}/L_{gg}	2.7 mH/1 mH
Filter capacitance	C_{gf}	6.9 μF
Grid inductance	L_s	4 mH
Grid resistance	R_s	1 Ω

TABLE II
PARAMETERS OF THE CONTROLLERS FOR FOUR CASES

Parameter \ Case	I	II	III	IV
k_{pic}/k_{vff}	6.0/0.9			
ω_{clp}	$2\pi\cdot50$ rad/s			
k_{iff}	0.8			0.15
k_{pvc}/k_{rvc}	0.05/6.0	0.05/6.0	0.05/6.0	0.05/6.0
k_{ppg}	6.0×10^{-3}	8.0×10^{-3}	2.4×10^{-3}	2.4×10^{-3}
k_{pqg}/k_{iqg}	2×10^{-3}/0.95	2×10^{-3}/1.35	2×10^{-3}/0.4	2×10^{-3}/0.4

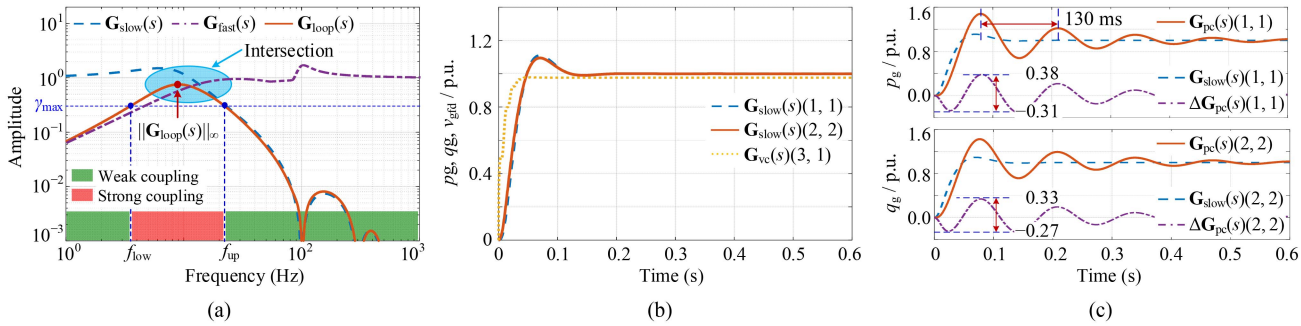

Fig. 7. Frequency and step responses of Case I. (a) Frequency responses of $\mathbf{G}_{\mathrm{slow}}(s)$, $\mathbf{G}_{\mathrm{fast}}(s)$, and $\mathbf{G}_{\mathrm{loop}}(s)$. (b) Step responses of $\mathbf{G}_{\mathrm{vc}}(s)$ and $\mathbf{G}_{\mathrm{slow}}(s)$. (c) Step responses of $\mathbf{G}_{\mathrm{slow}}(s)$, $\mathbf{G}_{\mathrm{pc}}(s)$, and $\Delta\mathbf{G}_{\mathrm{pc}}(s)$.

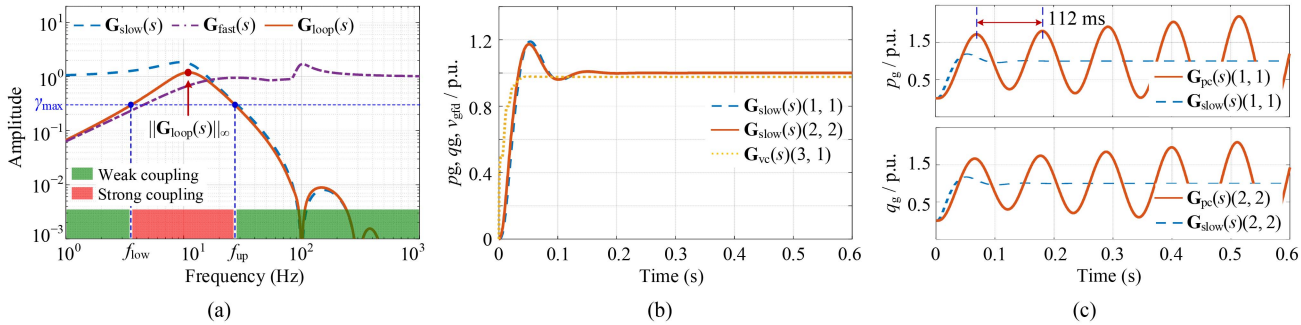

Fig. 8. Frequency and step responses of Case II. (a) Frequency responses of $\mathbf{G}_{\mathrm{slow}}(s)$, $\mathbf{G}_{\mathrm{fast}}(s)$, and $\mathbf{G}_{\mathrm{loop}}(s)$. (b) Step responses of $\mathbf{G}_{\mathrm{vc}}(s)$ and $\mathbf{G}_{\mathrm{slow}}(s)$. (c) Step responses of $\mathbf{G}_{\mathrm{slow}}(s)$ and $\mathbf{G}_{\mathrm{pc}}(s)$.

TABLE III
BANDWIDTHS OF POWER AND VOLTAGE LOOPS

Control loop \ Case	I	II	III	IV
Power loop	14.1 Hz	18.7 Hz	5.2 Hz	5.2 Hz
Voltage loop	15.0 Hz	15.0 Hz	15.0 Hz	6.2 Hz

highlighted. The fast subsystem $\mathbf{G}_{\mathrm{fast}}(s)$ is expressed as

$$\mathbf{G}_{\mathrm{fast}}(s) = \mathbf{C}_{\mathrm{pcal}}\Delta\mathbf{G}_{\mathrm{vc}}(s)(\mathbf{C}_{\mathrm{pcal}}\mathbf{G}_{\mathrm{vc0}})^{-1}. \tag{20}$$

By neglecting $\mathbf{G}_{\mathrm{fast}}(s)$, the slow subsystem $\mathbf{G}_{\mathrm{slow}}(s)$, which acts as a reduced-order simplification of $\mathbf{G}_{\mathrm{pc}}(s)$, is derived as

$$\begin{aligned}\mathbf{G}_{\mathrm{slow}}(s) = {} & [\mathbf{I}_2 + F_{\mathrm{d}}(s)F_{\mathrm{lp}}(s)\mathbf{C}_{\mathrm{pcal}}\mathbf{G}_{\mathrm{vc0}}\mathbf{C}_{\mathrm{vref}}\mathbf{K}_{\mathrm{pow}}(s)]^{-1} \\ & \times F_{\mathrm{d}}(s)F_{\mathrm{lp}}(s)\mathbf{C}_{\mathrm{pcal}}\mathbf{G}_{\mathrm{vc0}}\mathbf{C}_{\mathrm{vref}}\mathbf{K}_{\mathrm{pow}}(s).\end{aligned} \tag{21}$$

As observed, the full-order model of SPGFMCs has been formulated into an interconnection of slow and fast subsystems, with the slow subsystem typically employed in power controller design [19]. Notably, the fast subsystem dynamics are primarily governed by the voltage loop since it shares the same poles with $\mathbf{G}_{\mathrm{vc}}(s)$. This leads to a key observation: the decoupling of slow and fast subsystems implies the decoupling of the power and voltage control loops. In the following section, we will derive the decoupling criteria to complete the proposed robust singular perturbation method.

C. Proposed Decoupling Criteria of SPGFMCs

Following the approach of the SPT, the definition of the stability-based decoupling can be described as: if stable power and voltage control loops (or stable slow and fast subsystems) imply a stable full-order converter system, the two loops are considered decoupled in the sense of stability. In Fig. 5, the block diagram conforms to a standard robust control framework, with $\mathbf{G}_{\mathrm{fast}}(s)$ acting as an uncertainty [43]. When disconnecting $\mathbf{G}_{\mathrm{slow}}(s)$ and $\mathbf{G}_{\mathrm{fast}}(s)$, the relationship between $\Delta\mathbf{y}_{\mathrm{ipqg0}}$ and $\Delta\mathbf{y}_{\mathrm{ipqg}\Delta}$ is derived as

$$\Delta\mathbf{y}_{\mathrm{ipqg0}} = -\mathbf{G}_{\mathrm{slow}}(s)\Delta\mathbf{y}_{\mathrm{ipqg}\Delta}. \tag{22}$$

Consequently, we transform Fig. 5 into a negative-feedback form shown in Fig. 6, with $\Delta\mathbf{y}_{\mathrm{pqg\cdot ref}}$ set to zeros. $\mathbf{G}_{\mathrm{loop}}(s) = \mathbf{G}_{\mathrm{fast}}(s)\mathbf{G}_{\mathrm{slow}}(s)$ denotes the loop Laplacian matrix. Then, by use of the small-gain theorem in robust control, the stability-based decoupling criterion is derived as [43]

$$\|\mathbf{G}_{\mathrm{loop}}(s)\|_{\infty} = \|\mathbf{G}_{\mathrm{fast}}(s)\mathbf{G}_{\mathrm{slow}}(s)\|_{\infty} < 1 \tag{23}$$

where $\|\cdot\|_{\infty}$ denotes the H_{∞} norm of a Laplacian matrix and is defined as

$$\|\mathbf{G}_{\mathrm{loop}}(s)\|_{\infty} = \max_{\omega}\{\sigma_{\max}[\mathbf{G}_{\mathrm{loop}}(\mathrm{j}\omega)]\} \tag{24}$$

where ω is the angular frequency, $\sigma_{\max}(\cdot)$ denotes the maximum singular value, and $\sigma_{\max}[\mathbf{G}_{\mathrm{loop}}(\mathrm{j}\omega)]$ stands for the frequency response regarding the maximum singular value. Notably, $\sigma_{\max}[\mathbf{G}_{\mathrm{loop}}(\mathrm{j}\omega)]$ and $\|\mathbf{G}_{\mathrm{loop}}(s)\|_{\infty}$ are extensions of the

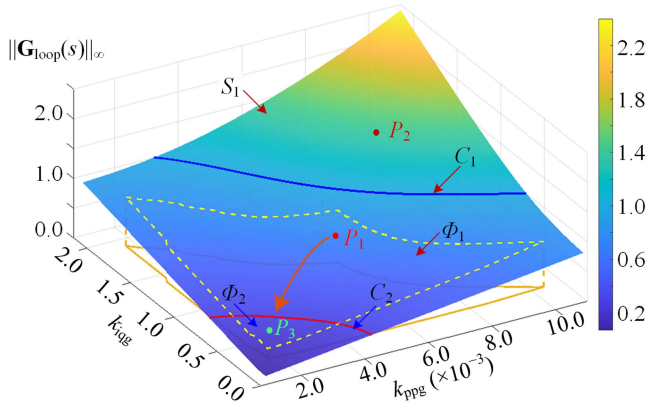

Fig. 9. Dependence of $\|\mathbf{G}_{\text{loop}}(s)\|_\infty$ on power control parameters k_{ppg} and k_{iqg}.

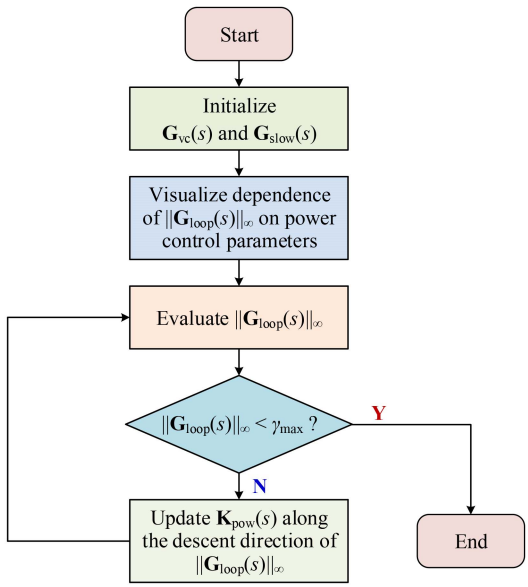

Fig. 10. Procedure to achieve decoupling design by use of the criteria.

amplitude-frequency plot and the maximum amplitude in the single-input single-output systems, respectively.

Remark 1: $\sigma_{\max}[\mathbf{G}_{\text{loop}}(\text{j}\omega)]$ quantifies the coupling between power and voltage loops at any given frequency. Larger values indicate stronger couplings. Clearly, $\|\mathbf{G}_{\text{loop}}(s)\|_\infty$ identifies the strongest coupling across all frequencies.

Beyond stability, the performance of SPGFMCs is also of practical importance. In this article, the performance-based decoupling is defined as: if $\mathbf{G}_{\text{pc}}(s)$ exhibits similar dynamic performance to the reduced-order model $\mathbf{G}_{\text{slow}}(s)$, the power and voltage control loops (or the slow and fast subsystems) are considered decoupled in the sense of performance. Since $\|\mathbf{G}_{\text{loop}}(s)\|_\infty$ quantifies the maximum coupling over all frequencies, a sufficiently small $\|\mathbf{G}_{\text{loop}}(s)\|_\infty$ implies effective decoupling. Consequently, the performance-based criterion is expressed as

$$\|\mathbf{G}_{\text{loop}}(s)\|_\infty = \|\mathbf{G}_{\text{fast}}(s)\mathbf{G}_{\text{slow}}(s)\|_\infty < \gamma_{\max} \tag{25}$$

where $\gamma_{\max}$ denotes a positive parameter smaller than one. Based on many tests, the parameter $\gamma_{\max}$ can be selected smaller than 0.3 to achieve decoupling regarding performance.

According to matrix theory, criterion (25) is satisfied if the following inequality holds for every ω:

$$\sigma_{\max}\left[\mathbf{G}_{\text{slow}}(\text{j}\omega)\right] \le \gamma_{\max}/\,\sigma_{\max}\left[\mathbf{G}_{\text{fast}}(\text{j}\omega)\right]. \tag{26}$$

Remark 2: From (26), reducing the amplitude of $\mathbf{G}_{\text{slow}}(s)$ or $\mathbf{G}_{\text{fast}}(s)$ helps satisfy (25). Since they are determined by the power and voltage loops, respectively, the proposed method supports the independent design of the two loops.

The criteria in (23) and (25), along with the inequality in (26), constitute the theoretical foundation of the robust singular perturbation method. Notably, although the decoupling criteria are presented on SPGFMCs, they can be extended to three-phase converters.

IV. Coupling Analysis and Decoupling Design of SPGFMCs Via the Proposed Method

In this section, the coupling between power and voltage control loops is analyzed using the proposed criteria, and the procedure for decoupled controller design is presented.

A. Coupling Mechanism Analysis Using the Criteria

Fig. 7 (Case I) shows how the criteria effectively reveal the coupling mechanism between control loops. The plant and controller parameters are listed in Tables I and II, respectively. In this case, the current controller parameters are designed according to [44] and [45] to regulate the converter-side currents and ensure adequate active damping. k_{vff} and k_{pic} are tuned to 0.9 and 6.0, respectively, ensuring that the minimum damping ratio among all closed-loop poles is no less than 0.28. For voltage control, appropriate voltage tracking performance and sufficient stability margin are required [18], [46]. The grid-side current feedforward coefficient is set to 0.8 to mitigate the influence of external current disturbances on voltage control. k_{pvc} and k_{rvc} of the voltage PR regulator are tuned to 0.05 and 6.0, respectively, yielding a voltage control bandwidth of 15.0 Hz and a phase margin of 56 °.

In Fig. 7(a), the frequency responses of $\mathbf{G}_{\text{slow}}(s)$, $\mathbf{G}_{\text{fast}}(s)$, and $\mathbf{G}_{\text{loop}}(s)$ are plotted, where f_{low} and f_{up} are the lower and upper bounds satisfying (25). As shown, $\mathbf{G}_{\text{slow}}(s)$ and $\mathbf{G}_{\text{fast}}(s)$ exhibit low-pass and high-pass characteristics, respectively. Based on (26), this results in a low magnitude of $\mathbf{G}_{\text{loop}}(s)$ at both low and high frequencies, indicating weak coupling as per *Remark 1*. In the frequency range where $\mathbf{G}_{\text{slow}}(s)$ and $\mathbf{G}_{\text{fast}}(s)$ intersect, neither of them is sufficiently attenuated, resulting in a high amplitude of $\mathbf{G}_{\text{loop}}(s)$ and implying stronger coupling.

In Case I, $\|\mathbf{G}_{\text{loop}}(s)\|_\infty = 0.75$ denotes the maximum coupling. Through computation, the bandwidths of power and voltage loops are 14.1 Hz and 15.0 Hz, respectively, as shown in Table III. According to the criterion in (23), we conclude that stability-based decoupling can still be achieved even when the two loops have comparable bandwidths.

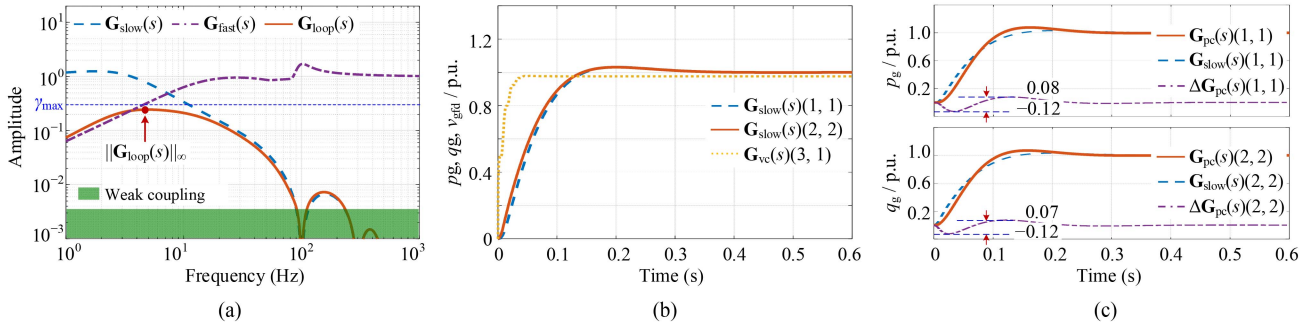

Fig. 11. Frequency and step responses of Case III. (a) Frequency responses of $\mathbf{G}_{\rm slow}(s)$, $\mathbf{G}_{\rm fast}(s)$, and $\mathbf{G}_{\rm loop}(s)$. (b) Step responses of $\mathbf{G}_{\rm vc}(s)$ and $\mathbf{G}_{\rm slow}(s)$. (c) Step responses of $\mathbf{G}_{\rm slow}(s)$, $\mathbf{G}_{\rm pc}(s)$, and $\Delta\mathbf{G}_{\rm pc}(s)$.

Fig. 7(b) and (c) illustrates the time-domain responses of Case I. In Fig. 7(b), the step responses of individual voltage and power loops are depicted, with $\mathbf{G}_{\rm slow}(s)(1, 1)$ and $\mathbf{G}_{\rm slow}(s)(2, 2)$ representing the reduced-order active and reactive power transfer functions. Fig. 7(c) shows the step responses of $\mathbf{G}_{\rm pc}(s)$, $\mathbf{G}_{\rm slow}(s)$, and their difference $\Delta\mathbf{G}_{\rm pc}(s)$. As predicted, the full-order system is stable. However, since $\|\mathbf{G}_{\rm loop}(s)\|_\infty$ fails to meet the performance-based criterion, an oscillation with a period of 130 ms appears in $\mathbf{G}_{\rm pc}(s)$, and the maximum deviation between $\mathbf{G}_{\rm pc}(s)$ and $\mathbf{G}_{\rm slow}(s)$ reaches 38%.

To validate the effectiveness of the criteria in predicting system instability, we intentionally increased the power control parameters $k_{\rm ppg}$ and $k_{\rm iqg}$, as shown in Case II in Table II. The results are depicted in Fig. 8. In this case, $\|\mathbf{G}_{\rm loop}(s)\|_\infty = 1.19$, which indicates the maximum coupling and violates the stability-based criterion. Based on the step responses in Fig. 8(b) and (c), we find that although power and voltage loops are individually stable, the SPGFMC exhibits oscillation and instability. These findings highlight the necessity of the proposed method in reliable controller design.

B. Decoupled Control Loop Design

As described in Remark 2, the power and voltage loops can be individually designed. Fig. 9 depicts the dependence of $\|\mathbf{G}_{\rm loop}(s)\|_\infty$ on power control parameters $k_{\rm ppg}$ and $k_{\rm iqg}$, with the voltage control parameters predesigned as in Case I. In this figure, the surface S_1 describes how $\|\mathbf{G}_{\rm loop}(s)\|_\infty$ varies with $k_{\rm ppg}$ and $k_{\rm iqg}$. Curves C_1 and C_2 are contour lines where $\|\mathbf{G}_{\rm loop}(s)\|_\infty$ satisfies (23) and (25), respectively. Region Φ_1 indicates the satisfactory power-loop performance designed using $\mathbf{G}_{\rm slow}(s)$, with a rise time under 150 ms and overshoot below 15%. Region Φ_2 is the intersection of Φ_1 and the area where $\|\mathbf{G}_{\rm loop}(s)\|_\infty < 0.3$. Points P_1 and P_2 correspond to Cases I and II, respectively.

Based on Fig. 9, an iterative design procedure is presented in Fig. 10, where the power control parameters are tuned for decoupling. The flowchart begins with the initialization of the voltage and power loops. Then, using the visualized parameter dependence, $\|\mathbf{G}_{\rm loop}(s)\|_\infty$ is evaluated and compared against the decoupling threshold. If not met, the power control parameters are updated along a descent direction of $\|\mathbf{G}_{\rm loop}(s)\|_\infty$.

Using the design procedure, we obtain a decoupled set of power control parameters, represented by point P_3 in Φ_2 and corresponding to Case III in Table II. The analytical results are depicted in Fig. 11. Fig. 11(a) shows that the power and voltage loops have been effectively decoupled across all frequencies, with $\|\mathbf{G}_{\rm loop}(s)\|_\infty$ reduced to 0.24. Fig. 11(b) and (c) further validates that the step responses of $\mathbf{G}_{\rm slow}(s)$ and $\mathbf{G}_{\rm pc}(s)$ are closely matched, with the maximum deviation between $\mathbf{G}_{\rm pc}(s)$ and $\mathbf{G}_{\rm slow}(s)$ reducing to 12%. In Case III, the bandwidths of power and voltage loops are 5.2 Hz and 15.0 Hz, respectively, yielding a bandwidth ratio of approximately three. This result is significantly less conservative than the conventional tenfold bandwidth separation.

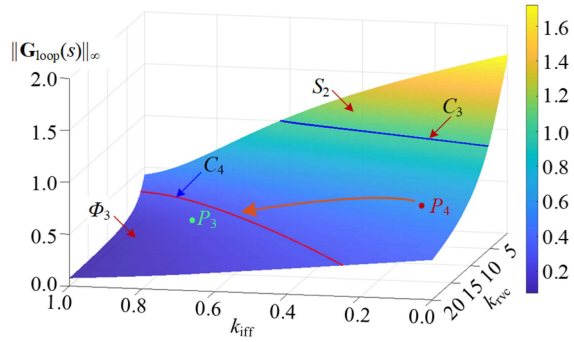

Fig. 12. Dependence of $\|\mathbf{G}_{\rm loop}(s)\|_\infty$ on voltage control parameters $k_{\rm rvc}$ and $k_{\rm iff}$.

Fig. 12 shows the dependence of $\|\mathbf{G}_{\rm loop}(s)\|_\infty$ on voltage control parameters $k_{\rm rvc}$ and $k_{\rm iff}$, with the power control parameters fixed as in Case III. In this figure, the surface S_2 describes how $\|\mathbf{G}_{\rm loop}(s)\|_\infty$ varies with $k_{\rm rvc}$ and $k_{\rm iff}$. Curves C_3 and C_4 denote contour lines where $\|\mathbf{G}_{\rm loop}(s)\|_\infty$ equals 1 and 0.3, respectively. Region Φ_3 is the intersection of S_2 and the area where $\|\mathbf{G}_{\rm loop}(s)\|_\infty < 0.3$.

Following a similar procedure to Fig. 10, the decoupling between power and voltage loops can also be realized by tuning voltage control parameters. Notably, the grid current feedforward is highly beneficial for decoupling. In Fig. 12, point P_4 corresponds to Case IV in Table II, where $k_{\rm iff}$ is reduced to 0.15 and other parameters are the same as those in Case III. The analytical results in Fig. 13(a) demonstrate that the decrease of $k_{\rm iff}$ leads to $\|\mathbf{G}_{\rm loop}(s)\|_\infty$ rising to 0.82. Although the system is stable, a relatively large $\|\mathbf{G}_{\rm loop}(s)\|_\infty$ indicates a strong coupling regarding performance. In Fig. 13(c), $\mathbf{G}_{\rm pc}(s)$ exhibits an oscillation with a period of 256 ms, and the maximum deviation between $\mathbf{G}_{\rm pc}(s)$ and $\mathbf{G}_{\rm slow}(s)$ is 43%.

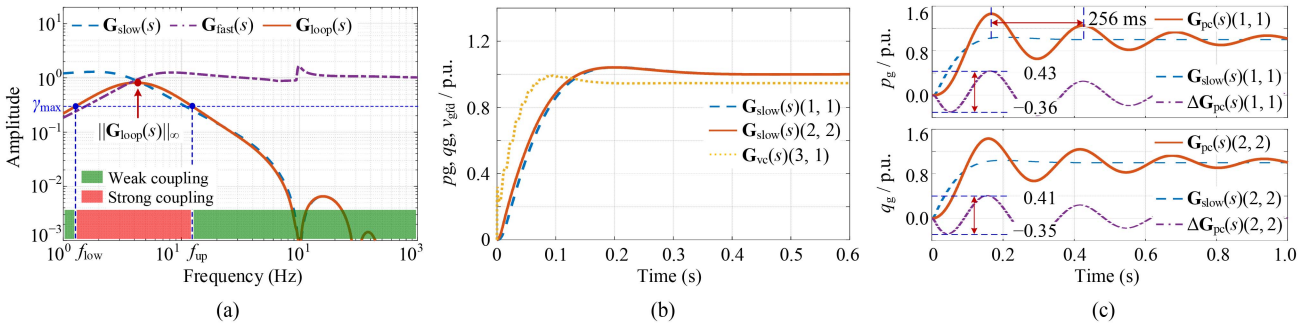

Fig. 13. Frequency and step responses of Case IV. (a) Frequency responses of $\mathbf{G}_{\rm slow}(s)$, $\mathbf{G}_{\rm fast}(s)$, and $\mathbf{G}_{\rm loop}(s)$. (b) Step responses of $\mathbf{G}_{\rm vc}(s)$ and $\mathbf{G}_{\rm slow}(s)$. (c) Step responses of $\mathbf{G}_{\rm slow}(s)$, $\mathbf{G}_{\rm pc}(s)$, and $\Delta\mathbf{G}_{\rm pc}(s)$.

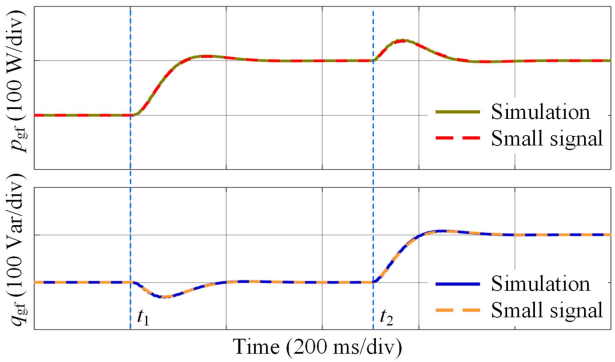

Fig. 14. Comparison between power-device-level simulation results and theoretical small-signal responses.

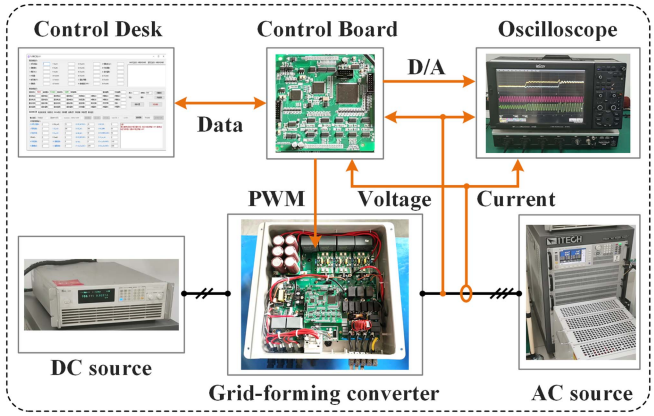

Fig. 15. Photo of the experimental setup.

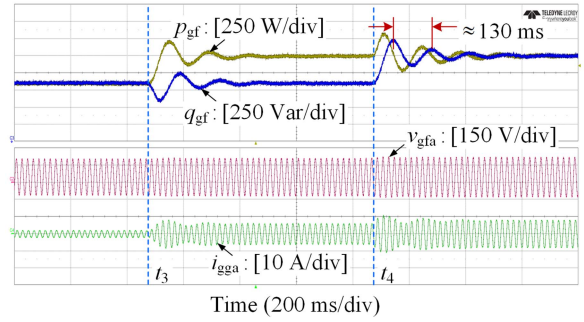

Fig. 16. Experimental results of Case I.

V. Simulation and Experimental Validations

In this section, simulation results verify the accuracy of the full-order small-signal model, and experimental results validate the effectiveness of the proposed robust singular perturbation method. The plant and control parameters are detailed in Tables I and II, respectively.

A. Verification of the Small-Signal Modeling

Since accurate modeling is a prerequisite for the proposed method, we first validate the accuracy of the small-signal model. Fig. 14 compares the power-device-level simulation results of the SPGFMC with the theoretical step responses of the small-signal model $\mathbf{G}_{\rm pc}(s)$. The control parameters are specified as those in Case III. At t_1 and t_2, step increases of 100 W and 100 Var are applied to $p_{\rm g^*ref}$ and $q_{\rm g^*ref}$, respectively. As observed, the theoretical small-signal model demonstrates strong agreement with the power-device-level simulation in both active and reactive power responses. This confirms the accuracy of the developed small-signal model.

B. Verification of the Decoupling Method

The experimental setup used for validation is shown in Fig. 15. The dc power source (Chroma 62150H-1000S) is utilized to supply the SPGFMC prototype, and the ac programmable source (ITECH IT7625) emulates the ideal power grid. All the controllers in Fig. 1 are implemented in a control board with a digital signal processor (Texas Instruments TMS320F28374S). In the following, experimental investigations are carried out for each of the four cases.

Fig. 16 shows the experimental results of Case I, showcasing the waveforms of $p_{\rm gf}$, $q_{\rm gf}$, $v_{\rm gfa}$, and $i_{\rm gga}$. Initially (before t_3), the reference values $p_{\rm g^*ref}$ and $q_{\rm g^*ref}$ are set to 100 W and 100 Var, respectively. At t_3, $p_{\rm g^*ref}$ steps up to 500 W, followed by a step increase of $q_{\rm g^*ref}$ to 500 Var at t_4. As anticipated from the theoretical analysis, the converter maintains stable operation, indicating that the stability-based decoupling has been achieved. However, since the criterion in (25) is not met, the waveforms of $p_{\rm gf}$ and $q_{\rm gf}$ exhibit undesirable oscillations with a period of 130 ms, similar to those of $\mathbf{G}_{\rm pc}(s)$ in Fig. 7(c). This indicates

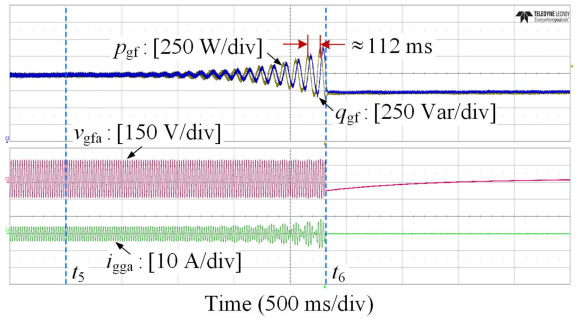

Fig. 17. Experimental results of Case II.

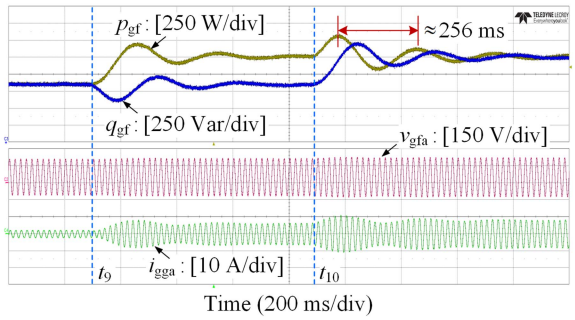

Fig. 19. Experimental results of Case IV.

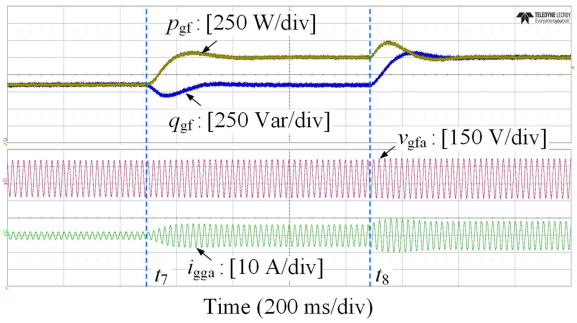

Fig. 18. Experimental results of Case III.

performance-based coupling, which is not fully addressed in Case I.

Fig. 17 presents the results for Case II, which are deliberately designed to further examine the predictive capability of the stability-based criterion. Prior to t_5, the control parameters from Case I are retained to ensure initial stability. At t_5, the parameters are switched to those of Case II. As shown, the converter exhibits a gradual loss of stability, culminating in system shutdown at t_6. The oscillation period of approximately 112 ms is consistent with that observed in Fig. 8(c), which corroborates the validity of the stability-based criterion in predicting system instability.

The experimental results of Case III are presented in Fig. 18, where the decoupling design is theoretically achieved using the proposed method. In this experiment, the step changes of $p_{g\cdot ref}$ and $q_{g\cdot ref}$ are set identically to those of Case I. As observed, the converter remains stable, and the waveforms of p_{gf} and q_{gf} closely match the theoretical results of $\mathbf{G}_{slow}(s)$ and $\mathbf{G}_{pc}(s)$ in Fig. 11. Accordingly, the decoupling between power and voltage loops regarding both stability and performance is successfully realized. Moreover, these results confirm that we derive an accurate reduced-order model of the SPGFMC by decoupled controller design.

Fig. 19 presents the experimental results of Case IV to validate the impact of grid-current feedforward on decoupling. In this case, the grid-current feedforward coefficient is set to 0.15. The testing conditions of $p_{g\cdot ref}$ and $q_{g\cdot ref}$ are the same as those of Case III. Since the stability-based criterion is satisfied, the converter remains stable. However, the experimental waveforms of p_{gf} and q_{gf} behave differently from those of $\mathbf{G}_{slow}(s)$ in Fig. 13, implying a failure in decoupling regarding performance. The oscillation period of approximately 256 ms coincides with the waveforms in Fig. 13(c). Therefore, the grid current feedforward can significantly enhance decoupling between power and voltage loops.

Collectively, these results validate the effectiveness of the proposed robust singular perturbation method, including the proposed criteria and design procedure.

VI. Conclusion

In this article, we propose a robust singular perturbation method for single-phase grid-forming converters to achieve coupling analysis and decoupling design of power and voltage loops. Two decoupling criteria, regarding system stability and performance, are derived by treating the fast subsystem of the converter model as an uncertainty. Compared with conventional singular perturbation theory, the proposed criteria provide a quantified coupling metric between the outer and inner control loops at each frequency point. For practical applications, the significance of this work lies in the following aspects.

1) It effectively addresses the performance degradation and instability caused by the coupling effect between power and voltage control loops.
2) It enables independent design of the power and voltage controllers, offering a less conservative decoupling condition than the conventional tenfold bandwidth separation.
3) It achieves accurate model reduction that further supports system-level investigations in microgrids and large-scale grid-forming converter systems.

The effectiveness of the theoretical analyses and decoupling design method is validated by simulation and experimental results. Moreover, although the proposed method is developed based on a single-phase system and a specific controller structure, it can be extended to three-phase systems and a variety of controller forms with multiloop coupling problems. As indicated by the derivation in Section III, establishing a small-signal model is a prerequisite for the proposed method. Once the model is constructed, the time-scale analysis can be performed, and the decoupling criteria remain applicable.

$$
\begin{aligned}
p_{\mathrm{g}} &= \frac{1}{2}[v_{\mathrm{gf}} i_{\mathrm{gg}} + \eta(v_{\mathrm{gf}})\eta(i_{\mathrm{gg}})] \\
&= \frac{1}{2}\left(v_{\mathrm{gfd}}\cos\theta_{\mathrm{s}} - v_{\mathrm{gfq}}\sin\theta_{\mathrm{s}}\right)\left(i_{\mathrm{ggd}}\cos\theta_{\mathrm{s}} - i_{\mathrm{ggq}}\sin\theta_{\mathrm{s}}\right) + \frac{1}{2}\eta\left(v_{\mathrm{gfd}}\cos\theta_{\mathrm{s}} - v_{\mathrm{gfq}}\sin\theta_{\mathrm{s}}\right)\eta\left(i_{\mathrm{ggd}}\cos\theta_{\mathrm{s}} - i_{\mathrm{ggq}}\sin\theta_{\mathrm{s}}\right) \\
&= \frac{1}{4}v_{\mathrm{gfd}} i_{\mathrm{ggd}} + \frac{1}{4}v_{\mathrm{gfq}} i_{\mathrm{ggq}} + \frac{1}{4}\eta(v_{\mathrm{gfd}})\eta(i_{\mathrm{ggd}}) + \frac{1}{4}\eta(v_{\mathrm{gfq}})\eta(i_{\mathrm{ggq}}) + p_{\mathrm{g2}}\left(\cos 2\theta_{\mathrm{s}},\ \sin 2\theta_{\mathrm{s}}\right) \qquad (28) \\
q_{\mathrm{g}} &= \frac{1}{2}[\eta(v_{\mathrm{gf}}) i_{\mathrm{gg}} - v_{\mathrm{gf}}\eta(i_{\mathrm{gg}})] \\
&= \frac{1}{2}\eta\left(v_{\mathrm{gfd}}\cos\theta_{\mathrm{s}} - v_{\mathrm{gfq}}\sin\theta_{\mathrm{s}}\right)\left(i_{\mathrm{ggd}}\cos\theta_{\mathrm{s}} - i_{\mathrm{ggq}}\sin\theta_{\mathrm{s}}\right) - \frac{1}{2}\left(v_{\mathrm{gfd}}\cos\theta_{\mathrm{s}} - v_{\mathrm{gfq}}\sin\theta_{\mathrm{s}}\right)\eta\left(i_{\mathrm{ggd}}\cos\theta_{\mathrm{s}} - i_{\mathrm{ggq}}\sin\theta_{\mathrm{s}}\right) \\
&= \frac{1}{4}\eta(v_{\mathrm{gfq}}) i_{\mathrm{ggd}} - \frac{1}{4}\eta(v_{\mathrm{gfd}}) i_{\mathrm{ggq}} - \frac{1}{4}v_{\mathrm{gfd}}\eta(i_{\mathrm{ggq}}) + \frac{1}{4}v_{\mathrm{gfq}}\eta(i_{\mathrm{ggd}}) + q_{\mathrm{g2}}\left(\cos 2\theta_{\mathrm{s}},\ \sin 2\theta_{\mathrm{s}}\right). \qquad (29)
\end{aligned}
$$

APPENDIX

This appendix provides explicit derivations in Section II.

1) Derivation of power calculation

Given that v_{gf} and i_{gg} refer to α-axis coordinates, they can be expressed using respective dq-axis coordinates according to $\alpha\beta0$/$dq0$ transformation [40]

$$
\begin{cases} v_{\mathrm{gf}} = v_{\mathrm{gfd}}\cos\theta_{\mathrm{s}} - v_{\mathrm{gfq}}\sin\theta_{\mathrm{s}} \\ i_{\mathrm{gg}} = i_{\mathrm{ggd}}\cos\theta_{\mathrm{s}} - i_{\mathrm{ggq}}\sin\theta_{\mathrm{s}} \end{cases}. \qquad (27)
$$

According to the trigonometric formulas, we can derive the following equations: $\eta(\cos\theta_{\mathrm{s}}) = -\sin\theta_{\mathrm{s}}$, $\eta(\sin\theta_{\mathrm{s}}) = \cos\theta_{\mathrm{s}}$, $\sin^2\theta_{\mathrm{s}} = (1-\cos 2\theta_{\mathrm{s}})/2$, $\cos^2\theta_{\mathrm{s}} = (1+\cos 2\theta_{\mathrm{s}})/2$, and $\sin\theta_{\mathrm{s}}\cos\theta_{\mathrm{s}} = \sin 2\theta_{\mathrm{s}}/2$.

By use of (27) and the abovementioned equations, the calculations of p_{g} and q_{g} are derived in (28) and (29), shown at the top of this page, respectively. In (28) and (29), $p_{\mathrm{g2}}(\cos 2\theta_{\mathrm{s}}, \sin 2\theta_{\mathrm{s}})$ and $q_{\mathrm{g2}}(\cos 2\theta_{\mathrm{s}}, \sin 2\theta_{\mathrm{s}})$ represent the double-line-frequency power oscillations, which are functions of $\cos 2\theta_{\mathrm{s}}$ and $\sin 2\theta_{\mathrm{s}}$. The explicit expressions of p_{g2} and q_{g2} are not elaborated in this article for simplicity.

2) Derivations of the PR regulator in the virtual dq0 frame

The state-space models of the voltage PR regulator are identical for the α- and β-axes, and can be expressed as <?TeX

$$
\begin{aligned}
\frac{\mathrm{d}}{\mathrm{d}t}\mathbf{x}_{\mathrm{vpr}} &= \begin{bmatrix} 0 & 1 \\ -\omega_0^2 & -2\omega_{\mathrm{cr}} \end{bmatrix}\mathbf{x}_{\mathrm{vpr}} + \begin{bmatrix} 0 \\ 1 \end{bmatrix} e_{\mathrm{vgf}} \\
y_{\mathrm{vpr}} &= 2k_{\mathrm{rvc}}\omega_{\mathrm{cr}}\begin{bmatrix} 0 & 1 \end{bmatrix}\mathbf{x}_{\mathrm{vpr}} + k_{\mathrm{pvc}} e_{\mathrm{vgf}} \qquad (30)
\end{aligned}
$$

<?TeX where $\mathbf{x}_{\mathrm{vpr}}$ and y_{vpr} denote the state vector and the output, respectively.

In [39], the transformation of the state-space model of the *LCL* filter from the $\alpha\beta0$ frame to the $dq0$ frame is derived in detail. As observed in (1), the transformation from the $\alpha\beta0$ frame to the $dq0$ frame introduces two cross-coupling terms, ω_0 and $-\omega_0$, between the state variables in the d- and q-axes. Meanwhile, the remaining coefficients remain unchanged. This conclusion can be extended to the voltage PR regulator following a similar derivation. Therefore, its $dq0$-frame representation is obtained as

$$
\begin{aligned}
\frac{\mathrm{d}}{\mathrm{d}t}\mathbf{x}_{\mathrm{vprdq}} &= \begin{bmatrix} 0 & \omega_0 & 1 & 0 \\ -\omega_0 & 0 & 0 & 1 \\ -\omega_0^2 & 0 & -2\omega_{\mathrm{cr}} & \omega_0 \\ 0 & -\omega_0^2 & -\omega_0 & -2\omega_{\mathrm{cr}} \end{bmatrix}\mathbf{x}_{\mathrm{vprdq}} + \begin{bmatrix} 0 & 0 \\ 0 & 0 \\ 1 & 0 \\ 0 & 1 \end{bmatrix}\mathbf{e}_{\mathrm{vgfdq}} \\
\mathbf{y}_{\mathrm{vprdq}} &= 2k_{\mathrm{rvc}}\omega_{\mathrm{cr}}\begin{bmatrix} 0 & 0 & 1 & 0 \\ 0 & 0 & 0 & 1 \end{bmatrix}\mathbf{x}_{\mathrm{vprdq}} + k_{\mathrm{pvc}}\mathbf{e}_{\mathrm{vgfdq}}. \qquad (31)
\end{aligned}
$$

3) Derivations of $\boldsymbol{G}_{ic}(s)$, $\boldsymbol{G}_{vc}(s)$, and $\boldsymbol{G}_{pc}(s)$

First, we define three matrices in advance to facilitate the derivation. To be specific, $\mathbf{C}_{\mathrm{igi}} = [\mathbf{I}_2, \mathbf{0}_{2\times 2}, \mathbf{0}_{2\times 2}]$, $\mathbf{C}_{\mathrm{vgf}} = [\mathbf{0}_{2\times 2}, \mathbf{I}_2, \mathbf{0}_{2\times 2}]$, and $\mathbf{C}_{\mathrm{igg}} = [\mathbf{0}_{2\times 2}, \mathbf{0}_{2\times 2}, \mathbf{I}_2]$ are defined to extract $\Delta\mathbf{i}_{\mathrm{gidq}}$, $\Delta\mathbf{v}_{\mathrm{gfdq}}$, and $\Delta\mathbf{i}_{\mathrm{ggdq}}$ from $\Delta\mathbf{x}_{\mathrm{pdq}}$, respectively. $\mathbf{I}_2$ and $\mathbf{0}_{2\times 2}$ are 2×2 identity and zero matrices, respectively.

Combining (1), (2), (3), and the above notations, the current control loop $\mathbf{G}_{\mathrm{ic}}(s)$ shown in Fig. 3 is derived as

$$
\mathbf{G}_{\mathrm{ic}}(s) = k_{\mathrm{pic}}\mathbf{G}_{\mathrm{p}}(s)G_{\mathrm{d}}(s)\left[\mathbf{I}_2 + (k_{\mathrm{pic}}\mathbf{C}_{\mathrm{igi}} - k_{\mathrm{vff}}\mathbf{C}_{\mathrm{vgf}})\mathbf{G}_{\mathrm{p}}(s)G_{\mathrm{d}}(s)\right]^{-1}. \qquad (32)
$$

According to (4), (5), and the expression of $\mathbf{G}_{\mathrm{ic}}(s)$, the voltage control loop $\mathbf{G}_{\mathrm{vc}}(s)$ in Fig. 3 is further deduced as

$$
\mathbf{G}_{\mathrm{vc}}(s) = \mathbf{G}_{\mathrm{ic}}(s)\left\{\mathbf{I}_2 + \left[\mathbf{K}_{\mathrm{vpr}}(s)\mathbf{C}_{\mathrm{vgf}} - k_{\mathrm{iff}}\mathbf{C}_{\mathrm{igg}}\right]\mathbf{G}_{\mathrm{ic}}(s)\right\}^{-1}\mathbf{K}_{\mathrm{vpr}}(s). \qquad (33)
$$

Finally, by use of (6), (8), (11), (12), (13), and (33), the power control loop $\mathbf{G}_{\mathrm{pc}}(s)$ is derived as

$$
\begin{aligned}
\mathbf{G}_{\mathrm{pc}}(s) = &\left[\mathbf{I}_2 + F_{\mathrm{d}}(s)F_{\mathrm{lp}}(s)\mathbf{C}_{\mathrm{pcal}}\mathbf{G}_{\mathrm{vc}}(s)\mathbf{C}_{\mathrm{vref}}\mathbf{K}_{\mathrm{pow}}(s)\right]^{-1} \\
&\times F_{\mathrm{d}}(s)F_{\mathrm{lp}}(s)\mathbf{C}_{\mathrm{pcal}}\mathbf{G}_{\mathrm{vc}}(s)\mathbf{C}_{\mathrm{vref}}\mathbf{K}_{\mathrm{pow}}(s). \qquad (34)
\end{aligned}
$$

REFERENCES

[1] D. E. Olivares et al., "Trends in microgrid control," *IEEE Trans. Smart Grid*, vol. 5, no. 4, pp. 1905–1919, Jul. 2014.

[2] X. Fu et al., "Large-signal stability of grid-forming and grid-following controls in voltage source converter: A comparative study," *IEEE Trans. Power Electron.*, vol. 36, no. 7, pp. 7832–7840, Jul. 2021.

[3] Y. Li, Y. Gu, and T. Green, "Revisiting grid-forming and grid-following inverters: A duality theory," *IEEE Trans. Power Syst.*, vol. 37, no. 6, pp. 4541–4554, Nov. 2022.

[4] F. Zhang, H. Xin, D. Wu, Z. Wang, and D. Gan, "Assessing strength of multi-infeed LCC-HVDC systems using generalized short-circuit ratio," *IEEE Trans. Power Syst.*, vol. 34, no. 1, pp. 467–480, Jan. 2019.

[5] X. Gao, D. Zhou, A. Anvari-Moghaddam, and F. Blaabjerg, "Stability analysis of grid-following and grid-forming converters based on state-space modelling," *IEEE Trans. Ind. Appl.*, vol. 60, no. 3, pp. 4910–4920, May/Jun. 2024.

[6] W. Si and J. Fang, "Transient stability improvement of grid-forming converters through voltage amplitude regulation and reactive power injection," *IEEE Trans. Power Electron.*, vol. 38, no. 10, pp. 12116–12125, Oct. 2023.

[7] J. Rocabert, A. Luna, F. Blaabjerg, and P. Rodriguez, "Control of power converters in AC microgrids," *IEEE Trans. Power Electron.*, vol. 27, no. 11, pp. 4734–4749, Nov. 2012.

[8] R. Rosso, X. Wang, M. Liserre, X. Lu, and S. Engelken, "Grid-forming converters: Control approaches, grid-synchronization and future trends—A review," *IEEE Open J. Ind. Appl.*, vol. 2, pp. 93–109, 2021.

[9] K. Ahmed, M. Seyedmahmoudian, S. Mekhilef, N. M. Mubarak, and A. Stojcevski, "A review on primary and secondary controls of inverter-interfaced microgrid," *J. Modern Power Syst. Clean Energy*, vol. 9, no. 5, pp. 969–985, Sep. 2021.

[10] H.-P. Beck and R. Hesse, "Virtual synchronous machine," in *Proc. 9th Int. Conf. Elect. Power Qual. Utilization*, Barcelona, Spain, Oct. 2007, pp. 1–6.

[11] S. V. Dhople, B. B. Johnson, and A. O. Hamadeh, "Virtual oscillator control for voltage source inverters," in *Proc. 51st Annu. Allerton Conf. Commun., Control, Comput.*, 2013, pp. 1359–1363.

[12] J. Fang, W. Si, L. Xing, and S. M. Goetz, "Analysis and improvement of transient voltage stability for grid-forming converters," *IEEE Trans. Ind. Electron.*, vol. 71, no. 7, pp. 7230–7240, Jul. 2024.

[13] *IEEE Standard for Interconnection and Interoperability of Inverter-Based Resources (IBRs) Interconnecting with Associated Transmission Electric Power Systems*, IEEE Standard 2800-2022, pp. 1–180, Apr. 2022.

[14] D. Ríos-Castro, D. Pérez-Estévez, and J. Doval-Gandoy, "AC-voltage controller for grid-forming converters," *IEEE Trans. Power Electron.*, vol. 38, no. 4, pp. 4529–4543, Apr. 2023.

[15] P. C. Loh and D. G. Holmes, "Analysis of multiloop control strategies for *LC*/*CL*/*LCL*-filtered voltage-source and current-source inverters," *IEEE Trans. Ind. Appl.*, vol. 43, no. 5, pp. 1401–1407, Sep./Oct. 2007.

[16] D. B. Rathnayake and B. Bahrani, "Multivariable control design for grid-forming inverters with decoupled active and reactive power loops," *IEEE Trans. Power Electron.*, vol. 38, no. 2, pp. 1635–1649, Feb. 2023.

[17] W. Li and J. Fang, "A single-voltage-loop PI-controlled grid-forming converter with sufficient switching harmonic attenuation," in *Proc. IEEE Energy Convers. Congr. Expo.*, Nashville, TN, USA, 2023, pp. 3013–3020.

[18] T. Qoria, F. Gruson, F. Colas, X. Guillaud, M.-S. Debry, and T. Prevost, "Tuning of cascaded controllers for robust grid-forming voltage source converter," in *Proc. Power Syst. Comput. Conf.*, 2018, pp. 1–7.

[19] H. Deng, J. Fang, Y. Qi, Y. Tang, and V. Debusschere, "A generic voltage control for grid-forming converters with improved power loop dynamics," *IEEE Trans. Ind. Electron.*, vol. 70, no. 4, pp. 3933–3943, Apr. 2023.

[20] S. Eberlein and K. Rudion, "Small-signal stability modelling, sensitivity analysis and optimization of droop controlled inverters in LV microgrids," *Int. J. Elect. Power Energy Syst.*, vol. 125, Feb. 2021, Art. no. 106404.

[21] P. Kokotović, H. K. Khalil, and J. O'reilly, *Singular Perturbation Methods in Control: Analysis and Design*. Philadelphia, PA, USA: SIAM, 1999.

[22] S. Ahmed-Zaid, P. Sauer, M. Pai, and M. Sarioglu, "Reduced order modeling of synchronous machines using singular perturbation," *IEEE Trans. Circuits Syst.*, vol. 29, no. 11, pp. 782–786, Nov. 1982.

[23] Z. Zhang, D. Zhu, Y. Ma, X. Zou, J. Hu, and Y. Kang, "Singular perturbation model and transient stability analysis of grid-connected converter under weak grid faults," *Proc. CSEE*, vol. 43, no. 2, pp. 454–466, 2023.

[24] Z. Zhang, J. Fang, C. Zhang, C. Fu, H. Wang, and Y. Zhang, "Two-time scale model reduction and voltage controller design of grid-forming converters," in *Proc. IEEE Energy Convers. Congr. Expo.*, Phoenix, AZ, USA, 2024, pp. 735–739.

[25] W. Cai, R. Mallik, and B. Johnson, "Singular-perturbation-based control design of single-phase grid-forming inverters," in *Proc. IEEE Energy Convers. Congr. Expo.*, Phoenix, AZ, USA, 2024, pp. 893–900.

[26] R. Mallik, B. Majmunović, S. Dutta, G.-S. Seo, D. Maksimović, and B. Johnson, "Control design of series-connected PV-powered grid-forming converters via singular perturbation," *IEEE Trans. Power Electron.*, vol. 38, no. 4, pp. 4306–4322, Apr. 2023.

[27] M. Rasheduzzaman, J. A. Mueller, and J. W. Kimball, "Reduced-order small-signal model of microgrid systems," *IEEE Trans. Sustain. Energy*, vol. 6, no. 4, pp. 1292–1305, Oct. 2015.

[28] V. Mariani, F. Vasca, J. C. Vásquez, and J. M. Guerrero, "Model order reductions for stability analysis of islanded microgrids with droop control," *IEEE Trans. Ind. Electron.*, vol. 62, no. 7, pp. 4344–4354, Jul. 2015.

[29] A. Nayak, M. M. Rayguru, S. Mishra, and M. J. Hossain, "A quantitative approach for convergence analysis of a singularly perturbed inverter-based microgrid," *IEEE Trans. Energy Convers.*, vol. 36, no. 4, pp. 3016–3030, Dec. 2021.

[30] S. J. Chen and J. L. Lin, "Maximal stability bounds of singularly perturbed systems," *J. Franklin Inst.*, vol. 336, no. 8, pp. 1209–1218, Nov. 1999.

[31] S. Eberlein and K. Rudion, "Impact of inner control loops on small-signal stability and model-order reduction of grid-forming converters," *IEEE Trans. Smart Grid*, vol. 14, no. 4, pp. 2812–2824, Jul. 2023.

[32] T. Qoria, F. Gruson, F. Colas, X. Kestelyn, and X. Guillaud, "Analysis of the coupling between the outer and inner control loops of a grid-forming voltage source converter," in *Proc. 22nd Eur. Conf. Power Electron. Appl.*, 2020, pp. P.1–P.10.

[33] M. Kabalan, P. Singh, and D. Niebur, "Nonlinear Lyapunov stability analysis of seven models of a DC/AC droop controlled inverter connected to an infinite bus," *IEEE Trans. Smart Grid*, vol. 10, no. 1, pp. 772–781, Jan. 2019.

[34] S. D'Arco, J. A. Suul, and O. B. Fosso, "Small-signal modelling and parametric sensitivity of a virtual synchronous machine," in *Proc. Power Syst. Comput. Conf.*, Aug. 2014, pp. 1–9.

[35] S. D'Arco, J. A. Suul, and O. B. Fosso, "Automatic tuning of cascaded controllers for power converters using eigenvalue parametric sensitivities," *IEEE Trans. Ind. Appl.*, vol. 51, no. 2, pp. 1743–1753, Mar./Apr. 2015.

[36] D. Sivadas and K. Vasudevan, "Stability analysis of three-loop control for three-phase voltage source inverter interfaced to the grid based on state variable estimation," *IEEE Trans. Ind. Appl.*,, vol. 54, no. 6, pp. 6508–6518, Nov./Dec. 2018.

[37] J. Liu, Y. Xia, W. Wei, Q. Feng, and P. Yang, "Effect of control damping on small-signal stability of grid-forming VSCs considering interaction between inner and outer loops," *IEEE Trans. Power Electron.*, vol. 39, no. 6, pp. 7685–7695, Jun. 2024.

[38] Y. Tang, Z. Qin, F. Blaabjerg, and P. C. Loh, "DQ reference frame modeling and control of single-phase active power decoupling circuits," in *Proc. IEEE Appl. Power Electron. Conf. Expo.*, Piscataway, NJ, USA: IEEE Press, Mar. 2015, pp. 2725–2732.

[39] X. Ruan, X. Wang, D. Pan, D. Yang, W. Li, and C. Bao, *Control Techniques for LCL-Type Grid-Connected Inverters*. Singapore: Springer, 2018, pp. 143–144.

[40] J. Fang, H. Deng, and N. Tashakor et al., "State-space modeling and control of grid-tied power converters with capacitive/battery energy storage and grid-supportive services," *IEEE J. Emerg. Sel. Topics Power Electron.*, vol. 11, no. 1, pp. 234–250, Feb. 2023.

[41] L. Zhang, L. Harnefors, and H.-P. Nee, "Power-synchronization control of grid-connected voltage-source converters," *IEEE Trans. Power Syst.*, vol. 25, no. 2, pp. 809–820, May 2010.

[42] C. Zhang, S. Yu, K. Jiang, X. Ge, and J. Ma, "A fast instantaneous power calculation algorithm for single-phase rectifiers based on arbitrary phase-delay method," *IEEE Trans. Ind. Appl.*, vol. 55, no. 4, pp. 3935–3945, Jul./Aug. 2019.

[43] S. Skogestad and I. Postlethwaite, *Multivariable Feedback Control: Analysis and Design*, vol. 2. Princeton, NJ, USA: Citeseer, 2007.

[44] W. Chen, X. Zhou, and S. Lu, "A proportional and predictive capacitor-voltage feedforward method for *LCL*-filtered grid-tied inverters with inverter-side current feedback," in *Proc. IEEE Int. Conf. Predictive Control Elect. Drives Power Electron*, Jinan, China, 2021, pp. 770–776.

[45] J. Wang, J. D. Yan, L. Jiang, and J. Zou, "Delay-dependent stability of single-loop controlled grid-connected inverters with *LCL* Filters," *IEEE Trans. Power Electron.*, vol. 31, no. 1, pp. 743–757, Jan. 2016.

[46] Y. Han, A.-T. Jiang, E. A. A. Coelho, and J. M. Guerrero, "Optimal performance design guideline of hybrid reference frame based dual-loop control strategy for stand-alone single-phase inverters," *IEEE Trans. Energy Convers.*, vol. 33, no. 2, pp. 730–740, Jun. 2018.

Zicheng Zhang (Student Member, IEEE) received the B.Sc. degree in automation in 2014 and the M.Sc. degree in control engineering in 2017 from Shandong University, Jinan, China, where he is currently working toward the Ph.D. degree in control theory and control engineering.

His research interests include modelling, stability analysis, and control of grid-following and grid-forming power converters.

Chenghui Zhang (Fellow, IEEE) received the B.S. and M.S. degrees in automation engineering from the Shandong University of Technology, Jinan, China, in 1985 and 1988, respectively, and the Ph.D. degree in control theory and operational research from Shandong University, Jinan, China, in 2001.

In 1988, he was with Shandong University, where he is currently a Professor with the School of Control Science and Engineering. He is also the Chief Manager of Power Electronic Energy-saving Technology and Equipment Research Center of Education Ministry. His research interests include optimal control of engineering, power electronics and motor drives, energy-saving techniques, and time-delay systems.

Cheng Fu received the B.S. degree in automation and M.S. degree in the control science and engineering of Qingdao University, Qingdao, China, in 2016 and 2019, respectively, and the Ph.D. degree in power electronics from Shandong University, Jinan, China, in 2024.

He is currently a Distinguished Professor with the School of Automation, Qingdao University. His research interests include advanced control of power converters, applied nonlinear control, and intelligent systems.

Jingyang Fang (Senior Member, IEEE) received the B.Sc. and M.Sc. degrees in electrical engineering from Xi'an Jiaotong University, Xi'an, China, in 2013 and 2015, respectively, and the Ph.D. degree from the School of Electrical and Electronic Engineering, Nanyang Technological University, Singapore, in 2019.

Since 2021, he has been with the School of Control Science and Engineering, Shandong University as a Full Professor. His research interests include power quality control, stability analysis and improvement, renewable energy integration, and digital control in more-electronics power systems.